Graphene-assisted photothermal effect on promoting catalytic activity of layered MnO_2 for gaseous formaldehyde oxidation

Jinlong Wang[a,c], Gaoke Zhang[a,b,**], Pengyi Zhang[c,*]

[a] School of Resources and Environmental Engineering, Wuhan University of Technology, Wuhan, 430070, China
[b] State Key Laboratory of Silicate Materials for Architectures, Wuhan University of Technology, Wuhan, 430070, China
[c] State Key Joint Laboratory of Environment Simulation and Pollution Control, School of Environment, Tsinghua University, Beijing, 100084, China

ARTICLE INFO

ABSTRACT

It is an ideal approach to utilize solar energy instead of heat to drive catalytic reactions. Graphene exhibits a significant photothermal effect and is among the prominent candidates for the utilization of solar energy, especially that of near infrared radiation (NIR). Herein, a kind of graphene (disordered graphene nanoplatelet)-based MnO_2 nanohybrid (MnO_2-G) was prepared and investigated under irradiation of a xenon lamp for catalytic oxidation of gaseous formaldehyde. Compared to using only MnO_2, the MnO_2-G hybrid exhibited much higher activity, and the transformation rate of HCHO into CO_2 increased to 80%. The excellent activity of the MnO_2-G hybrid can be attributed to the synergistic photothermal effect between MnO_2 and graphene, which enhances the use of light, especially in the infrared region. Because of the high heat conducting ability of graphene, heat was rapidly transferred from the graphene nanoplatelet to MnO_2. Thus, the surface temperature of MnO_2 was even higher than that of solo graphene, and this in turn facilitated the activation of surface lattice oxygen. In addition, the chargeability of Mn atom increased because of the hybridization between MnO_2 and grapheme at interface. As a result, increased electron density on MnO_2-G surface facilitated the activation of oxygen molecules and the formation of superoxide radicals. This result demonstrates a novel approach for efficient use of inexhaustible solar energy, and the assistance of graphene photothermal effect in a traditional catalytic process is a promising strategy for improving catalytic efficiency of traditional thermo-catalysts.

1. Introduction

Formaldehyde (HCHO), which is one of the most prevalent indoor pollutants, needs to be treated to improve indoor air quality with the rapid urbanization in the world [1–4]. Catalytic oxidation process based on noble metals or transition metal oxides is the most convenient method for removing of HCHO from indoor air. Among them, noble-metal catalysts generally suffer from high cost and are susceptible to poisoning in practical conditions, thus their application is limited [5–11]. Transition metal oxide is an alternative catalyst which shows significant prospect [12–17]. However, the oxidation process originated from a redox cycle (oxygen activation and oxygen transfer) usually needs the assistance of extra energy, thus, inhibiting the wide application, especially for the real application in the indoor environment.

For catalytic processes, most of the catalytic oxidation needs to activate molecular oxygen, but activation of oxygen in a redox process generally requires additional energy. Solar energy, by far, is the largest

exploitable energy source, and attracts intense research, including its capture, conversion, and storage [18]. It is an ideal approach to utilize solar energy instead of heat to drive catalytic reactions. Recently, the emerging photothermal effect provides a new way to harvest solar energy specifically, narrow band gap metal oxides can be excited and heated by visible and infrared light) to promote catalytic reaction rates [19–21]. Manganese oxides are a prominent candidate because of their low cost and environmental compatibility [22–29]. More importantly, they possess strong photo absorption ability and exhibit a significant photothermal effect. Li et al. [30] recently reported that the temperature of MnO_2 can reach as high as 180 °C when irradiated by a xenon lamp, and this indicates significant potential in replacing the catalytic combustion technique. The temperature increase that occurs with solar light irradiation can be attributed to the heating effect of the energy released via the quick non-radiative recombination of the electron-hole pairs produced by the d-d transitions of Mn^{4+} because of the photon absorption [31]. In addition, Zheng et al. [32] also reported the solar

light driven thermocatalytic oxidation of volatile organic compounds (VOCs) in the decomposition of C_3H_8 and C_3H_6 over different type of tunnel structured manganese oxides. However, the strong absorption of solar light over MnO_2 mainly occurred on the UV, visible light and a small part of near Infrared radiation (NIR) region [30]. The Infrared light, which accounts for almost half of solar energy, has not been fully utilized by MnO_2. Thus, it is interesting to develop methods for increasing the utilization efficiency of solar light.

Efficient conversion of solar thermal energy relies on efficient photothermal conversion materials. Carbon-based materials, especially graphene, with broad spectral absorption properties and photothermal conversion properties are regarded as an ideal photothermal conversion material [33]. Even though the inherent mechanism of graphene photothermal effect is still unclear, its application has been extensively investigated. Dai et al. [34] reported that the ultrasmall reduced graphene oxide exhibited high NIR absorbance and the heat generated could be used for cancer treatment. In addition, the fabrication of graphene device was also successfully used for highly efficient solar thermal generation of clean water to solve the shortage of water resources [35]. The hierarchical graphene foam could even exhibit up to 93.4% of solar to thermal energy conversion efficiency [33]. Thus, it is possible to fabricate graphene based catalyst to fully utilize solar energy instead of heat to overcome the activation energy during catalytic oxidation process.

Lots of research works have been done on the synthetic control of graphene-MnO_2 composites. MnO_2 with nanoflower [36], nanowire [37], ultrathin layer [38], and nanorod structures [39] had been reported to be deposited on the surface of graphene. However, to the best of our knowledge, the assistance of graphene photothermal effect for catalytic process has not yet been explored. In this work, we fabricated a facile MnO_2-Graphene (MnO_2-G) via simple mechanical milling method. The preparation method was simple. However, the obtained composite consisted of close contacted graphene and MnO_2 as confirmed by TEM and XPS analysis. The MnO_2-G hybrid exhibited much higher activity than solo MnO_2, and the transformation rate of HCHO into CO_2 increased to 80%, during which MnO_2 provides active reaction sites for formaldehyde oxidation and graphene transfer photothermal energy to MnO_2. This synergistic interplay significantly enhances the reactions beyond the capability of conventional thermal-driven reactions.

2. Experimental section

2.1. Preparation of catalyst

All chemicals used here were analytical grade. $MnSO_4 \cdot H_2O$ and $KMnO_4$ were purchased from Beijing Chemical Reagent Co., Ltd. Graphene nanoplatelet aggregates (sub-micron particles, surface area 750 m^2/g) were obtained from Strem Chemicals Co., Ltd.

Layered MnO_2 was synthesized according to a procedure reported in literature [22]. $KMnO_4$ (1.5 g) and $MnSO_4 \cdot H_2O$ (0.275 g) were dissolved in 80 mL of deionized water. The solution was then transformed into a hydrothermal reactor and was kept at 240 °C for 24 h reaction. The precipitate was centrifuged, washed to remove possible residual impurities and then dried at 105 °C for 24 h. Finally, the obtained samples were calcined in a muffle furnace at 300 °C for 4 h.

Graphene-based nanohybrids (MnO_2-G) were obtained through mechanical milling method. Certain amounts of graphene and MnO_2 were ground in a mortar for 1 h to construct their close interface. For comparison, MnO_2-G sample with simple mixture was also prepared. The detailed information was illustrated in **Supporting Information**. Furthermore, mass ratio of graphene in MnO_2-G hybrids varied from 10% to 75%, and the hybrids (50 mg) were denoted as MnO_2-10%G, MnO_2-25%G, MnO_2-50%G, MnO_2-75%G. For convenience, if there is no specific description, "MnO_2-G" refers to the sample of "MnO_2-50%G".

2.2. Characterization

Scanning electron microscopy (SEM) was recorded on a JSM-5610LV microscope (JEOL, Japan). Transmission electron microscopy (TEM) was performed on a JEM-2100 F microscope (JEOL, Japan). X-ray diffraction (XRD) patterns of different samples were recorded on a D/MAX-RBD diffractometer (RIGAKU, Japan) using Cu Kα radiation (λ = 0.1542 nm). Raman spectra were recorded on an INVIA (RENIS-HAW, U.K.) with the excitation wavelength of 514.5 nm. Fourier transform infrared spectroscopy (FT-IR) was recorded on Nexus (Thermo Nicolet, U.S.A.) from 400 cm^{-1} to 4000 cm^{-1}. Diffuse reflectance UV–vis-Infrared absorption was performed on a Lambda 750 S spectrophotometer (PerkinElmer, U.S.A.). The temperature increase of different samples under a xenon lamp irradiation was detected on-line using a DT-1000 infrared thermometer (JTKY, China). X-ray photoelectron spectroscopy (XPS) analysis was conducted using an ESCALAB 250Xi X-ray photoelectron spectrometer (Thermo Fisher, USA) operated with a pass energy of 30 eV, using Al Kα (λ = 1486.7 eV) as an excitation X-ray source. ESR signals of radicals trapped by DMPO were recorded on a JEOL JES FA-200 (Japan) spectrometer at ambient temperature under photo-irradiation of a xenon lamp. Typical spectrometer parameters were as follows: centre field at 3378 G, sweep width of 100 G, microwave frequency of 9.440 GHz, modulation frequency 100 kHz, power 1 mW. DFT calculations were performed with the CASTEP package on the basis of the plane-wave-pseudo-potential approach. Geometry optimization was performed until the Hellmann-Feynman force on each atom was smaller than 0.02 eV·Å^{-1} during the atomic structure optimization.

2.3. Catalytic activity test

Catalytic activity of samples was evaluated in an 800 mL cylindrical stainless steel reactor with a quartz glass window fixed between the flange connections (**Figure S1**). Circulating water around the reactor was used to maintain the temperature of the reactor at 35 °C. Typically, samples (25 mg of MnO_2; 25 mg of graphene; 50 mg of MnO_2-G nanohybrid) were placed on the bottom of a glass Petri dish and covered with a glass slide. Then, 1.0 μL of HCHO (38%) solution was injected into the reactor. The initial concentration of HCHO was controlled to be around 250 ppm when HCHO was fully volatilized. A xenon lamp (AuLight, China) was placed above the reactor. The electrical output power of the xenon lamp was adjustable (70, 140, and 210 W). To evaluate the effect of wavelength, wavepass cutoff filters of 420 nm and 800 nm were placed between the xenon lamp and the quartz window. Concentration of HCHO and CO_2 were analyzed online using a photoacoustic IR multigas monitor (INNOVA air Tech Instruments Model 1412). The glass cover of the Petri dish was removed to start the catalytic oxidation of HCHO. Activity of different samples was compared in both dark and light conditions.

3. Results and discussion

3.1. Morphologies and physical/chemical structures

Morphologies of different samples were observed using SEM and TEM. The synthesized MnO_2 exhibited a morphology that was a nanoflower structure which was built up by many interleaving nanobelts with a width of approximately 20 nm (**Figure S2a** and Fig. 1a). The SEM image of commercial graphene showes aggregated sub-micron nanoplatelet structure with grain sizes in the range of 0.1–2 μm (**Figure S2b**). The surface of graphene was not smooth and the distorted edge of the nanoplatelet was constructed by flake-like thin graphene layers viewing from TEM and HRTEM image (Fig. 1c and d). The lattice fringe in graphene was not clear, indicating structural distortions occurred on the basal planes. In addition, only a small portion of surface exhibited diffraction fringe, separated by disordered regions, which was called
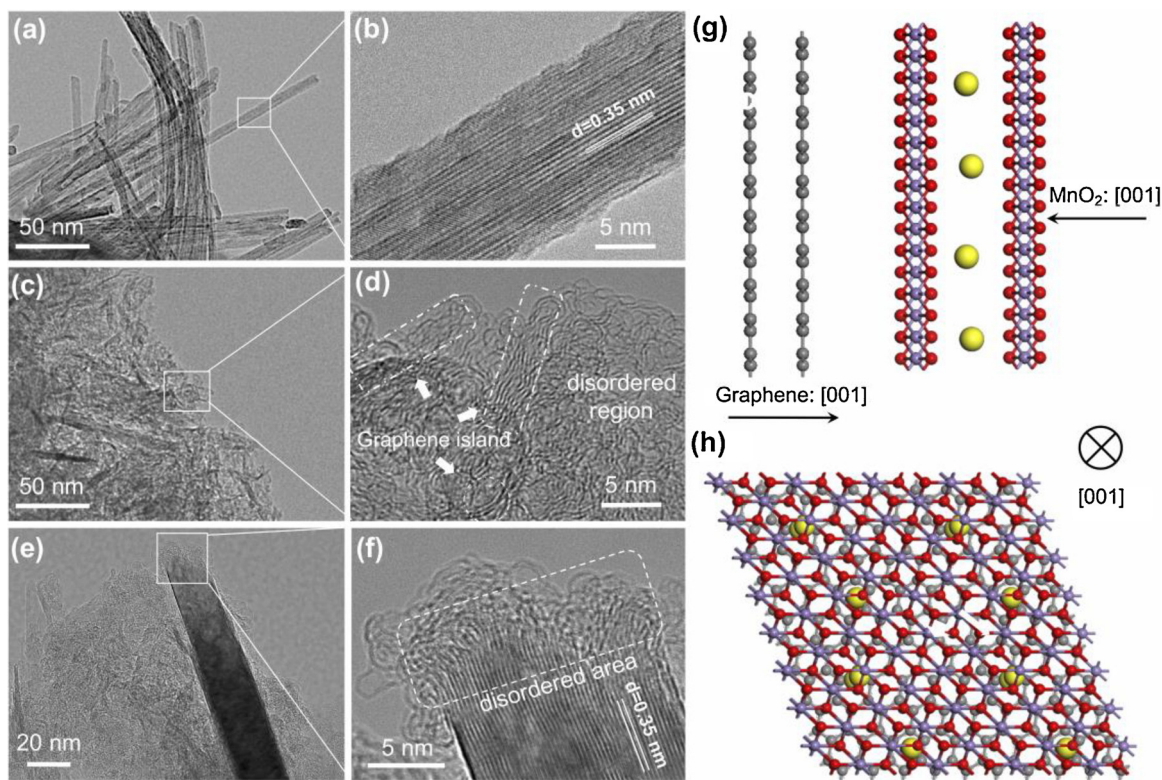
Fig. 1. TEM and HRTEM images of layered MnO_2 (a–b), Graphene (c–d), and MnO_2-G (e–f). Front (g) and top (h) views of simulated crystallographic structure of the MnO_2-G nanohybrid. Purple, red, and grey atoms represent Mn, O, and C, respectively. H_2O intercalated in the layers was relaxed.

graphene islands in the literature [21]. The electrons in the graphene islands behave like Dirac Fermions and the graphene islands could produce an ensemble effect of collective oscillation of electrons under specific range of irradiation wavelengths [40,41]. Both the MnO_2 nanobelt and graphene nanoplatelet were observed in the SEM image of the MnO_2-G nanohybrid (**Figure S2c**). Sub-micron graphene particles occupied the interspace of the interconnected network of MnO_2, and this resulted in better incorporation of MnO_2 and graphene, which is conducive to heat transfer between the two substances. The TEM and HRTEM images also indicated the close contact between MnO_2 and graphene (dashed square in Fig. 1e and 1f). The lattice fringe of 3.5 Å corresponding to the {002} planes of MnO_2 became obscure at the edge of the contacted interface, implying the edge of MnO_2 was covered with graphene. In addition, the simulated crystallographic structure of MnO_2-G nanohybrid viewed from front and top were given in Fig. 1g and h. The (001) surface of layered MnO_2 could directly attach with (001) surface of graphene via weak van der Waals force. Gan et al. explored the structure of MnO_2/Graphene interface via first-principles calculation and further indicated this possible crystallographic structure [42]. It was proved that the formation of the MnO_2/Graphene interface was an exothermic process and spin polarization occurred between the π and O 2p orbitals. The minimum value of interfacial binding energy of the integrated hybrid could be obtained when the interlayer distance was about 3.03 Å. Similar structure was also employed in the chemically integrated MnO_2/Graphene hybrid planar supercapacitor. Ultrathin MnO_2 nanosheets stacked on graphene directly and tightly, which diminished the interlayer space, significantly hindering the electrolyte ion diffusion [43]. To further confirm crystallographic structure of MnO_2-G, it was found that K/Mn atom ratio was far less than bulk for MnO_2 (K/Mn ratio: 0.21XPS vs 0.34EDS), proving K^+ was mainly in the bulk instead of on the outermost surface because the K^+ is highly soluble in water and can be depleted via repeated washing. Similar phenomenon was also observed on the surface of α-MnO_2, the 2×2 tunnels initially occupied by K^+ will become an

unoccupied open structure at the surface after washing [44]. Thus, it could be concluded that graphene contacted with layered MnO_2 directly at interface when the two components were integrated.

XRD patterns of different samples are shown in Fig. 2a. 2θ at 12.3°, 24.6°, 36.5° and 65.5° are characteristic diffraction peaks of layered MnO_2 (PDF 80–1098), and can be ascribed to (001), (002), (−111) and (020) crystal facets, respectively [45]. After incorporating MnO_2 into graphene, the broad lump peak over 15–30° was the typical diffraction peak of graphene [46]. The sharp peak located at 26.4° can be ascribed to the incompletely exfoliated graphite, corresponding to the (002) peak with an interlayer d-spacing of 0.34 nm [47]. In addition, the intensity and position of all of the diffraction peaks of MnO_2 in MnO_2-G nanohybrid did not change compared to the diffraction peaks of the pristine sample.

Raman spectroscopy was used to analyze the local structure of MnO_2 and graphene, and the result was shown in Fig. 2b. Three major peaks at 508, 576, and 641 cm^{-1} were observed on MnO_2 sample, which can be assigned to typical spectra of layered MnO_2 due to the vibration of Mn-O bond in [MnO_6] octahedral [48]. In the spectra of graphene sample, the D band at 1348 cm^{-1} indicated the typical structure of graphene, which was due to the edge distortions and topological defects.[46] The intensity ratio of I_D/I_G is an indicator of the disorder degree of sp^2 domains of graphene. The I_D/I_G intensity ratio of graphene varied differently when the two components were integrated. The I_D/I_G value of MnO_2-G was calculated to be 0.85, obviously lower than the 1.16 of graphene, indicating the degree of sp^2 domains decreased due to the possible chemical interaction between MnO_2 and graphene nanosheets.

In addition, the surface functional groups of different samples were investigated using FT-IR spectra (Fig. 2c). For MnO_2, the peak located at 523 cm^{-1} corresponded to Mn-O vibrations.[45] The strong peak at 3447 cm^{-1} was attributable to the stretching vibrations of adsorbed water molecules and structural OH group, and the peak at 1634 cm^{-1} can be attributed to OH bending vibrations [49]. The bands of the
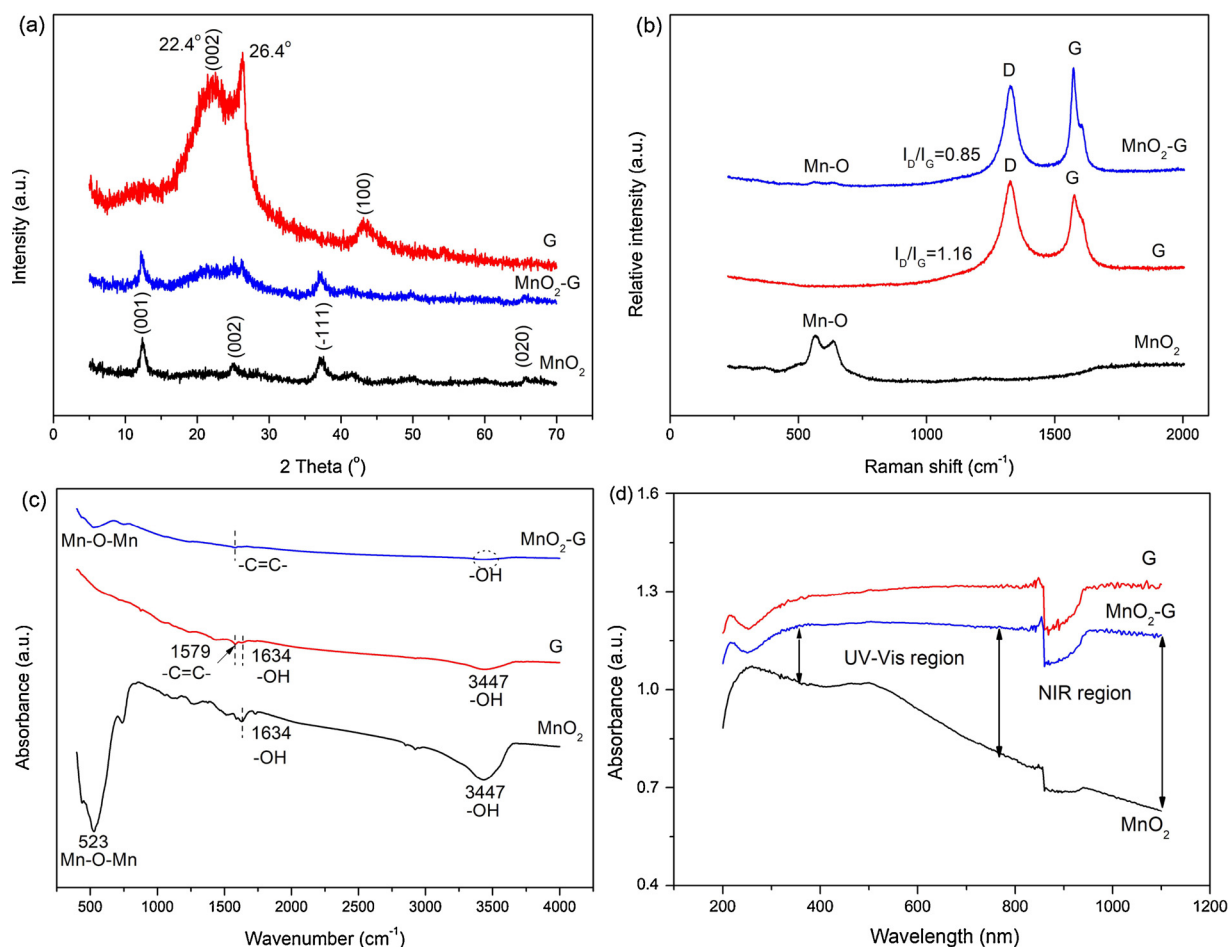
Fig. 2. Characterizations of layered MnO_2, graphene and MnO_2-G nanohybrids. (a) XRD patterns, (b) Raman spectra, (c) FT-IR spectra, and (d) UV–vis-NIR spectra.

graphene sample at $1579\ cm^{-1}$ can be attributed to the carbon skeletal vibrations [50]. In addition, surface hydroxyl was also observed on the surface of graphene. The appearance of hydroxyl species is due to in-complete chemical reduction of graphene oxides in the synthesis of graphene. In the case of MnO_2-G, Mn-O-Mn vibrations, and surface hydroxyl groups were both observed.

In order to reveal light response of different samples, diffuse re-flectance UV–vis-NIR spectra were recorded to reveal light responses of different samples (Fig. 2d). MnO_2 showed strong absorption in the UV and visible region. However, when the spectra were extended to the near infrared region, the absorbance of MnO_2 decreased. Similar phe-nomenon was also observed in the octahedral layered MnO_2 with na-noflower structure [30]. Compared to the solo MnO_2, the MnO_2-G composite did not show enhanced absorption in the UV–vis region due to the strong spectra absorption of MnO_2 in this region. However, the absorption in the near-infrared region (780–1100 nm) was greatly en-hanced because of the introduction of graphene.

The Mn 2p spectra of MnO_2 and MnO_2-G nanohybrid were con-ducted and displayed in Fig. 3a. The Mn $2p_{3/2}$ spectrum was decon-voluted into two peaks, which are ascribed to Mn^{3+} and Mn^{4+}, re-spectively [25]. The binding energy of Mn $2p_{3/2}$ peak shifted to lower value for MnO_2-G (642.0 eV) compared to that of MnO_2 (642.3 eV). The downshift results were because of an increase in the π electron cloud density that originated from the introduction of graphene [45]. As a result, the chargeability of Mn atoms increased due to the interfacial charge transfer from graphene. For comparison, Mn $2p_{3/2}$ XPS spectra of Graphene-MnO_2 composite synthesized via simple mixed method (MnO_2-G-M) were also provided. The binding energy of Mn $2p_{3/2}$ in MnO_2-G-M (642.2 eV) was close to the pure MnO_2, indicating no

obvious changes of MnO_2 surface chemical state could be observed. To further confirm this hypothesis, we visualized the charge redistribution at the interfaces (Fig. 3b). It was observed that the big π-bond in gra-phene was strongly affected by O atoms in MnO_2 slab, resulting in the decreased electronic localization and extended π conjugated systems. Gan et al. also illustrated this electron transfer process using spin-po-larized band structure. The MnO_2 conduction band was fully spin-po-larized and the bottom of it crossed the Fermi energy. In addition, spin polarization at the Dirac point arised in graphene by proximity coupling to MnO_2, resulting in the strong interaction between the π and O 2p orbitals [42]. The unique electronic structure would contribute to the electron transfer, resulting in high-density electrons in MnO_2 when contacting with graphene.

3.2. Activity and stability

Activities of MnO_2, graphene, and the MnO_2-G nanohybrid are compared in Fig. 4. Since the reaction time (40 min) was fixed in the experiments, the differences in ΔHCHO and ΔCO_2 were also given in Table 1. In the absence of light irradiation, the concentration of HCHO decreased from 250 ppm to 80 ppm over the MnO_2 sample. Corre-spondingly, the generation of CO_2 was about 110 ppm, and this was somewhat lower than the decreased amount of HCHO (170 ppm), in-dicating some intermediates (e.g., formate, carbonates, bicarbonates, DOM) formed on the MnO_2 surface [23–25]. Graphene could also ad-sorb HCHO, and thus, the concentration of HCHO decreased from 250 ppm to 180 ppm in the dark. The graphene used here had the specific surface area that was as high as 750 m^2/g, which may facilitate the adsorption of HCHO. However, no CO_2 was observed in this case,
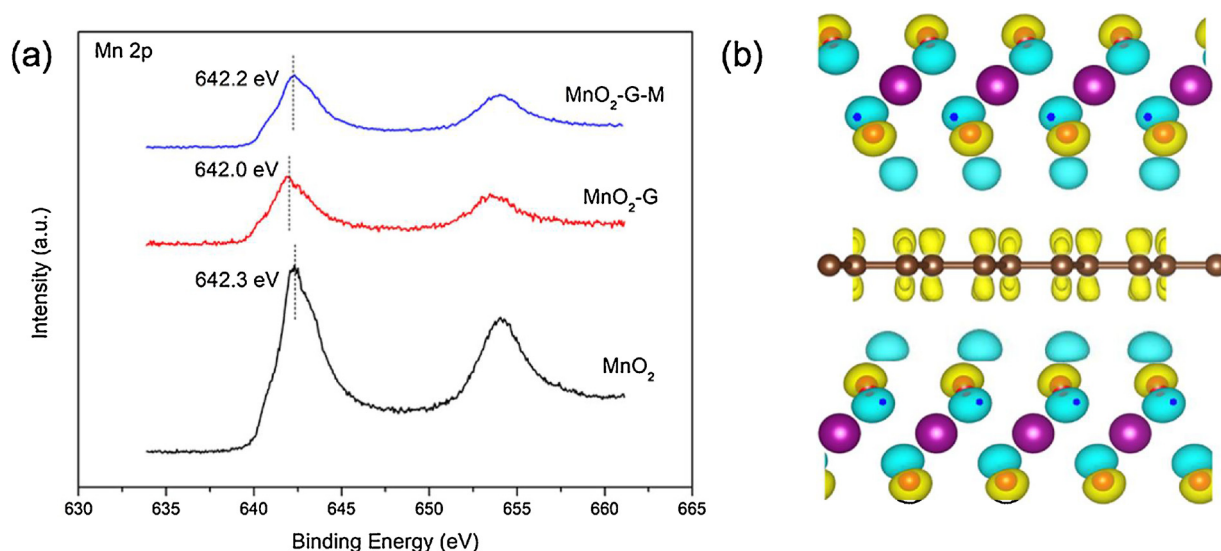
Fig. 3. (a) XPS spectra of Mn $2p_{3/2}$. (b) Charge difference distribution of MnO_2-G. Yellow region denotes charge depletion while blue denotes accumulation. The purple, red, and grey atoms represent Mn, O, and C, respectively.

indicating that HCHO was only adsorbed by graphene. For the MnO_2-G hybrid, the decreased content of HCHO was 200 ppm, and this could be attributed to the combined contributions of MnO_2 catalytic oxidation and graphene adsorption. However, the generation of CO_2 (90 ppm) was even lower than that with sole MnO_2. It meant that no other promotion effect occurred and HCHO adsorbed on graphene did not transfer to the active site of MnO_2 for further oxidation.

Interestingly, significant change occurred under the full solar spectral irradiation of the xenon lamp. For MnO_2, the concentration of HCHO decreased to 190 ppm which could be attributed to the photo-thermal effect of MnO_2 under UV–vis-IR irradiation. Meanwhile, the generation of CO_2 (150 ppm) also increased, implying that light enhanced the activity of MnO_2 because of its transformed thermal effect. Similar solar light promotion effect has also been observed in layered MnO_2 with nanoflower structure for CO oxidation [30]. When the graphene sample was irradiated under the xenon lamp, the amount of physically adsorbed HCHO decreased and CO_2 generation was not observed. This means that xenon light does not excite graphene to facilitate photocatalytic oxidation of HCHO, and because of light absorption, an increase in temperature inhibited the physical adsorption of HCHO by graphene. However, when the MnO_2-G hybrid was exposed to the light, the removal efficiency of HCHO greatly increased. The

Table 1
The value of ΔHCHO and $ΔCO_2$ over three different samples under dark or light reaction.

	Dark		Full light	
	$-ΔHCHO$(ppm)	$ΔCO_2$ (ppm)	$-ΔHCHO$ (ppm)	$ΔCO_2$ (ppm)
G	90	0	40	0
MnO_2	170	110	190	150
MnO_2-G	200	90	218	270

generation of CO_2 is about 270 ppm, which was an 80% increase compared to that obtained with just MnO_2 (The value of 270 ppm was a little higher than the theoretical value because of the release of adsorbed HCHO from the inner wall; the instrument could not detect.). It could be concluded that the presence of graphene facilitated rather than inhibited the generation of CO_2. The presence of graphene in the MnO_2-G nanohybrid should have a positive effect on the HCHO catalytic oxidation process.

Catalytic activity of the MnO_2-G nanohybrid was measured under different ranges of irradiation (Fig. 5) to understand better the assistance of the photothermal effect. MnO_2-G showed enhanced catalytic
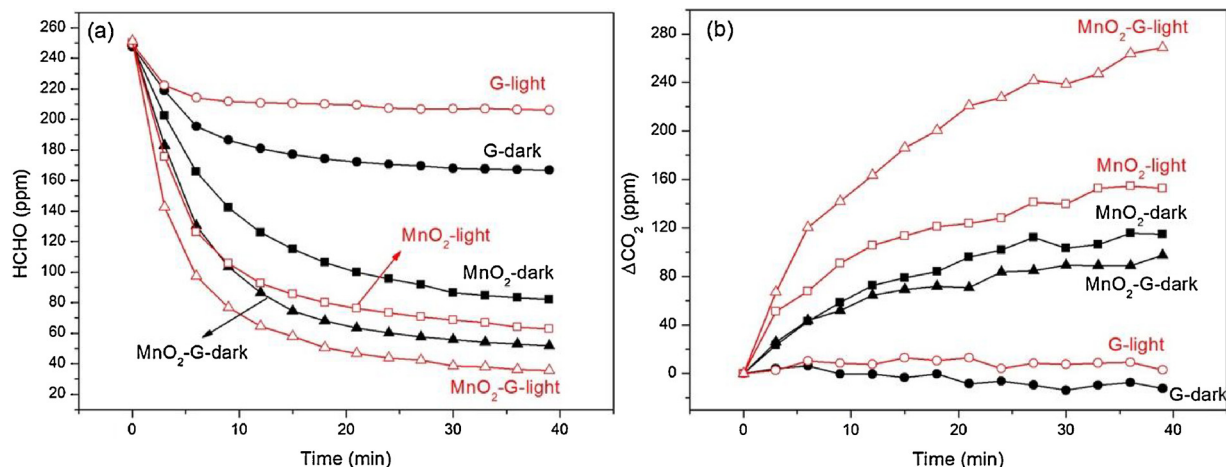

Fig. 4. Concentration changes of HCHO (a) and $ΔCO_2$(b) as a function of reaction time for layered MnO_2, graphene, and the MnO_2-G hybrid with (denoted as -light) and without (denoted as -dark) Xe lamp irradiation.
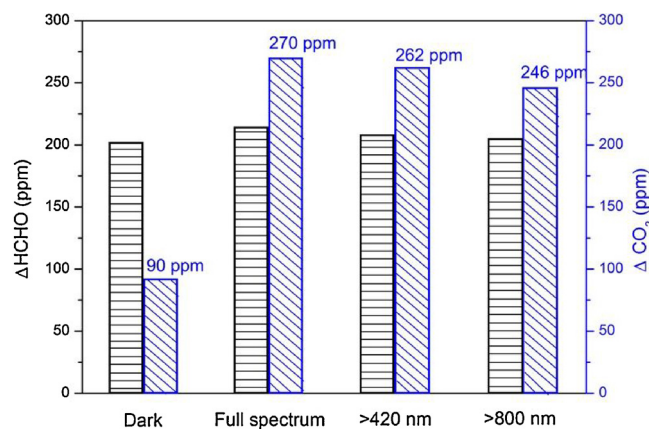
Fig. 5. Catalytic activity of MnO_2-G under different conditions (dark, full light, visible-infrared and infrared regions).

Fig. 6. Temperature changes of layered MnO_2, graphene, and the MnO_2-G hybrid under 70 W Xe lamp irradiation.

activity under full, visible-infrared and infrared irradiation as compared to dark conditions. The complete mineralization, presence of intermediates, and physical adsorption of graphene are responsible for the high removal of HCHO. Because of the synergistic physical adsorption and chemical adsorption of graphene and MnO_2 to HCHO, the decreased content of HCHO did not vary too much, however, the content of generated CO_2 changed significantly. The generation of CO_2 over MnO_2-G exhibited as high as 270 ppm under full light irradiation. Remarkably, even only under infrared irradiation with a wavelength above 800 nm, it still exhibited a very high catalytic activity with the generation of CO_2 as high as 246 ppm. In addition, the CO_2 generation only increased 16 ppm when the light source involved with infrared as well as visible region. Considering the spectrum distribution, most of the light energy is mainly distributed in the high wavelength region, which might decrease the contribution of UV and visible region during irradiation. In addition, the energy excitation from ground state to its excited state via the d-d transition on MnO_2 could be occurred at infrared region. The narrow bandgap inevitably leads to a considerable decrease in the utilization efficiency of solar energy as all photon energy in excess of exciting energy is lost via electron-phonon interactions. Thus, it could be concluded that the contribution of the wavelength region mainly comes from the infrared parts.

Considering of the decreased content of active MnO_2 components and the enhancement of the photothermal effect introduced by the increased content of graphene with the change of graphene mass ratio in MnO_2-G integrated sample, the ratio between MnO_2 and graphene has an optimal value. As shown in **Figure S3**, the effect of graphene mass ratio in MnO_2-G hybrid was also investigated. MnO_2-75%G had the lowest HCHO removal efficiency, and this should be because of the deficient amount of MnO_2. The HCHO removal efficiency was almost the same for MnO_2-10%G, MnO_2-25%G and MnO_2-50%, which may because of the balanced effects of enhanced MnO_2 catalytic activity and decreased physical adsorption of graphene. However, the CO_2 generation was quite different for the four samples, which followed the order of MnO_2-50%G > MnO_2-25%G > MnO_2-10%G > MnO_2-75%G. In addition, the electrical output power of the xenon lamp was adjusted (70, 140, and 210 W) to study the effects of UV–vis-NIR light intensity on the photothermal catalytic process. As shown in **Figure S4**, with an increase in power, the HCHO removal efficiency was further increased over MnO_2-50%G hybrid catalyst, implying that catalytic activity was dependent of light irradiation.

The stability of catalysts and their efficiency are very important for practical applications of the catalysts. To investigate the stability of MnO_2-G hybrid in the decomposition of HCHO, the test was cycled 6 times and the results are shown in **Figure S5**. The decrease of HCHO concentration and simultaneous increase of CO_2 in every test was almost the same as those in the first test, suggesting excellent stability of
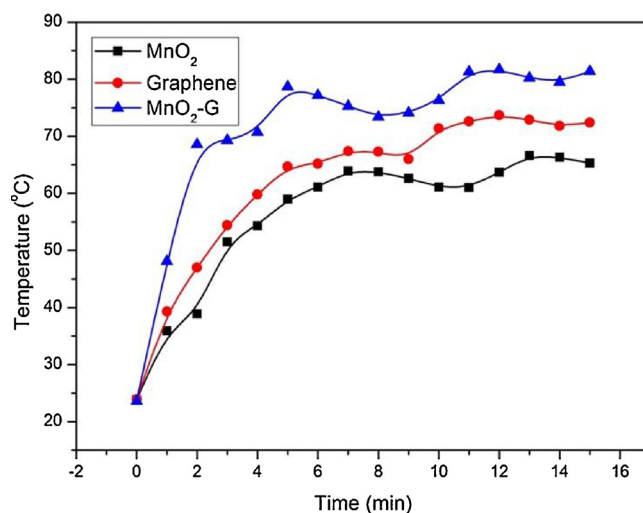
MnO_2-G for HCHO oxidation under light irradiation. This result implies that MnO_2-G hybrid shows a great potential as an efficient photothermal catalyst for of HCHO removal in the long-term practical use.

3.3. Mechanism

The highly efficient catalytic activity of MnO_2-G hybrid under light irradiation is considered to originate from photothermal catalysis. To confirm this assumption, the surface temperature of different samples under the irradiation of a xenon lamp was measured using an infrared thermometer (Fig. 6). When the lamp was turned on, the surface temperature of MnO_2 quickly increased in 5 min and stabilized at ~ 60 °C after that. The increased temperature could be attributed to the heating effect due to the quick non-radiative recombination of the electron-hole pairs produced by the d-d transitions of Mn ions upon the absorption of photons [30]. The result in this study confirms that MnO_2 can transform solar light including UV–vis and a part of infrared light to thermal energy, thus resulting in a significant increase in temperature. As for graphene, the temperature reached to ~ 70 °C because of the strong absorption of NIR light. At present, very little is known about the inherent mechanism of photothermal effect in graphene.

The proposed explanation of localized surface plasmon resonances (which is similar to the explanation for Ag, Au, or Cu metals) seems acceptable. Strong interactions occur between graphene and low-frequency photons at infrared frequencies, generating heat through plasma photothermal conversion [40]. The photothermal effect of graphene under UV and visible irradiation is not obvious [51]. When NIR light illuminates the graphene, the absorbed photons excite the valence band electrons to generate free carriers in the conduction band (electrons) and the valance band (holes). Such excited-state free charge carriers relax to the ground state by emitting optical phonons because of a large energy window of the Dirac-like electronic states. Extensive interaction between electrons and lattice vibrations leads to a hot lattice temperature. Strong electron-phonon interactions in graphene result in efficient photothermal energy conversions. When MnO_2 was incorporated into graphene, the temperature reached as high as 80 °C, even higher than that of graphene, which can be explained by the heat transfer from graphene to MnO_2 due to the excellent thermal conductivity of graphene [52], leading to the higher temperature than sole graphene. Thus, MnO_2-G nanohybrid not only fully absorbs solar spectra, but also efficiently transfers heat energy to MnO_2 for HCHO oxidation. It is known that the HCHO oxidation over MnO_2 follows a metal-assisted Mars-van Krevelen (MvK) mechanism, in which adsorption and dissociation of O_2 and activation of surface lattice oxygen
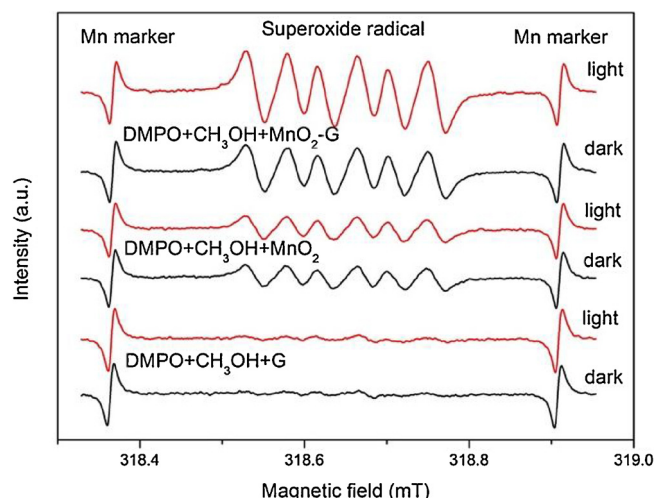
Fig. 7. DMPO spin-trapping ESR spectra with (denoted as -light) and without (denoted as -dark) Xe lamp irradiation at room temperature over MnO_2, graphene and MnO_2-G samples.

occur [53]. The increase in temperature over MnO_2-G nanohybrid under light irradiation might facilitate the mobility of surface lattice oxygen.

Oxygen activation includes not only surface lattice oxygen but also molecular O_2 according to the MvK theory. $\cdot O_2$ could be activated by trapping electrons and be present in the form of superoxide radical (i.e. $\cdot O_2^-$) to play a role in during the catalytic process [10,54]. Herein, $\cdot O_2^-$ formed over different samples and was detected via ESR using DMPO and as the spin-trap reagent in methanol solution (Fig. 7). For graphene, the characteristic six peaks of DMPO-$\cdot O_2^-$ did not appear. Even though the charge carrier concentration was high on graphene surface because of conjugated π bonds, the superoxide radicals that formed on graphene seemed negligible with or without light irradiation, which meant that O_2 was not easily activated on graphene surface. The $\cdot O_2^-$ intensity with an increase in irradiation time over graphene sample was also detected (**Figure S6a**), and no obvious $\cdot O_2^-$ accumulation was observed. For MnO_2, $\cdot O_2^-$ was detected and showed relatively high intensity even in the dark. However, the intensity of the radical signal seemed unchanged when the light was illuminated (**Figure S6b**). It is known that during irradiation d-d electronic transitions in MnO_2 occur due to its partially filled d-orbitals. As reported in the literature, the position of MnO_2 conduction band was about 0.57 eV, which was not low enough to reduce molecular O_2 (-0.33 eV) [55]. Thus, it could be concluded that the generation of $\cdot O_2^-$ was not a photocatalytic process, while it might be originated from thermal excitation. Deficiency sites (manganese vacancy or oxygen vacancy) were widely existed on the surface of MnO_2, which could act as active sites for activating O_2 into electrophilic $\cdot O_2^-$ species [56]. Mn^{3+} existed on

the surface of layered MnO_2, exhibiting a strong Jahn-Teller effect. If O_2 gas stands at the top of or lies around Mn^{3+} ions close to the surface oxygen vacancy, the corresponding electronic transfer occurred from 3d orbital of Mn^{3+} to the 2p orbital of O, forming $\cdot O_2^-$ species. Similar phenomenon was also observed on oxygen vacancy existed TiO_2 sample [57]. When MnO_2 was integrated with graphene, higher intensity of $\cdot O_2^-$ ERP signal was observed compared to that of MnO_2 under dark condition (Fig. 7). The hybridization between MnO_2 and graphene favored electron transport, resulting in higher electron density on surface. Similar phenomenon was also observed on the Na-Pd/TiO_2, negatively charged and well-dispersed Pd species could be helpful for the activation of chemisorbed oxygen [7]. When the MnO_2-G was illuminated, it was noted that the intensity of $\cdot O_2^-$ signal obviously increased once. The $\cdot O_2^-$ intensity reached to the maximum value in 60 s, indicating the electron transfer in short time (**Figure S6c**). NIR irradiation heats up the graphene sheets because of its photothermal effect. The generated heat rapidly transfers from graphene nanoplatelet to MnO_2 due to the graphene's excellent thermal conducting ability and intimate contact between MnO_2 and graphene. As a result, the temperature of MnO_2 was further increased, both activating the surface lattice oxygen and gas phase O_2, facilitating dissociation of O_2 by charge transfer from manganese to the orbitals of O_2, reducing the energy barrier of the O_2 molecules adsorption energy, thus, enhancing the catalyst activity.

On the basis of above results and discussions, the mechanism was proposed (Fig. 8). MnO_2 itself can oxidize HCHO at ambient temperature without irradiation, however, the efficiency is restricted due to the lack of energy input to overcome the reaction barrier. Graphene could contact with layered MnO_2 directly at interface via weak van der Waals force when the two components were integrated. After the light, especially near infrared part, illuminated the sample, the electrons could obtain more energy and moved faster on the graphene nanoplatelet, heating up the graphene due to its photothermal effect. The generated heat rapidly transfers from graphene nanoplatelet to MnO_2 due to the graphene's excellent thermal conducting ability and intimate contact between MnO_2 and graphene. As a result, the temperature of MnO_2 was further increased, i.e., the surface lattice oxygen was activated. In addition, this integrated structure also affected the electron structure of MnO_2-G nanohybrid by interfacial hybridization, which decreased the electronic localization and subsequently extended the π conjugated systems. As a result, the chargeability of Mn atoms increased due to the interfacial charge transfer from graphene, which could act as active sites for activating O_2 into electrophilic $\cdot O_2^-$ species. The activation of oxygen molecules and lattice oxygen together facilitate the whole catalytic activity.

4. Conclusion

A graphene-based MnO_2 hybrid was synthesized via a facile mechano-chemical method. Under irradiation, MnO_2-G exhibited much higher activity for formaldehyde decomposition than solo MnO_2 or solo
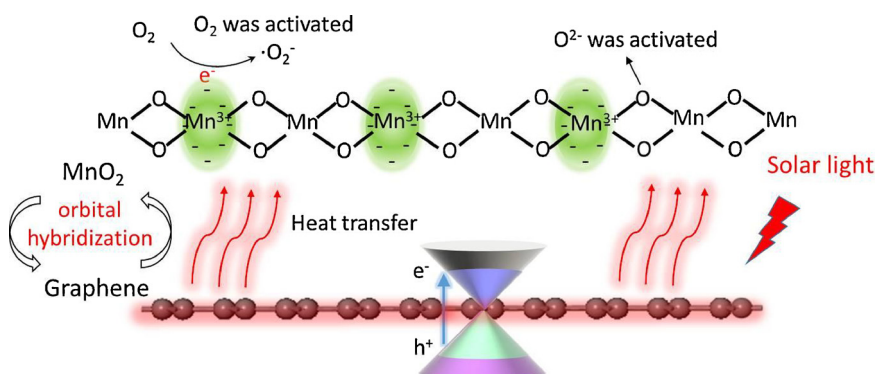

Fig. 8. Mechanism of enhanced HCHO catalytic oxidation activity over MnO_2-G nanohybrid under light irradiation.

graphene. The enhanced catalytic activity of the MnO_2-G nanohybrid originated from the synergistic photothermal effect between MnO_2 and graphene. The generated heat rapidly transferred from the graphene nanoplatelet to MnO_2 because of the high conducting ability of graphene, and the surface temperature of MnO_2 was further increased. In addition, the chargeability of Mn atom increased because of the hybridization between MnO_2 and grapheme at interface. The thermal transfer as well as electron transfer together facilitated the activation of surface active site for the oxidation of gaseous HCHO. This work offers a new strategy for the utilization of solar energy by combining catalyst with photothermal material, considerably increasing the catalyst surface temperature and accordingly accelerating the catalytic reaction. The synthetic method can be easily enforced for large-scale application. And the structure of graphene-based composite could be further optimized to improve the catalytic efficiency.

Acknowledgement

Appendix A. Supplementary data

Supplementary material related to this article can be found, in the online version, at doi:https://doi.org/10.1016/j.apcatb.2018.08.008.

References

[1] T. Salthammer, S. Mentese, R. Marutzky, Formaldehyde in the indoor environment, Chem. Rev. 110 (2010) 2536–2572.

[2] C. Jiang, D. Li, P. Zhang, J. Li, J. Wang, J. Yu, Formaldehyde and volatile organic compound (VOC) emissions from particleboard: identification of odorous compounds and effects of heat treatment, Build. Environ. 117 (2017) 118–126.

[3] Y. Zhang, J. Mo, C. Weschler, Reducing health risks from indoor exposures in rapidly developing urban China, Environ. Health Persp. 121 (2013) 751–755.

[4] J. Ye, X. Zhu, C. Cheng, J. Yu, C. Jiang, Few-layered graphene-like boron nitride: a highly efficient adsorbent for indoor formaldehyde removal, Environ. Sci. Technol. Lett. 4 (2017) 20–25.

[5] C. Zhang, F. Liu, Y. Zhai, H. Ariga, N. Yi, Y. Liu, K. Asakura, M.F. Stephanopoulos, H. He, Alkali-metal-promoted Pt/TiO2 opens a more efficient pathway to formaldehyde oxidation at ambient temperatures, Angew. Chem. Int. Ed. 51 (2012) 9628–9632.

[6] J. Wang, J. Li, P. Zhang, G. Zhang, Understanding the "seesaw Effect" of Interlayered K^+ with Different Structure in Manganese Oxides for the Enhanced Formaldehyde Oxidation 224 (2018), pp. 863–870.

[7] C. Zhang, Y. Li, Y. Wang, H. He, Sodium-Promoted Pd/TiO2 for catalytic oxidation of formaldehyde at ambient temperature, Environ. Sci. Technol. 48 (2014) 5816–5822.

[8] H. Tan, J. Wang, S. Yu, K. Zhou, Support morphology-dependent catalytic activity of Pd/CeO2 for formaldehyde oxidation, Environ. Sci. Technol. 49 (2015) 8675–8682.

[9] B. Chen, C. Shi, M. Crocker, Y. Wang, A. Zhu, Catalytic removal of formaldehyde at room temperature over supported gold catalysts, Appl. Catal. B: Environ. 132 (2013) 245–255.

[10] Y. Chen, Z. Huang, M. Zhou, P. Hu, C. Du, L. Kong, J. Chen, X. Tang, The active sites of supported silver particle catalysts in formaldehyde oxidation, Chem. Commun. 52 (2016) 9996–9999.

[11] S. Huang, X. Zhu, B. Cheng, J. Yu, C. Jiang, Flexible nickel foam decorated with Pt/NiO nanoflakes with oxygen vacancies for enhanced catalytic formaldehyde oxidation at room temperature, Environ. Sci-Nano 4 (2017) 2215–2224.

[12] Y. Sekine, Oxidative decomposition of formaldehyde by metal oxides at room temperature, Atmos. Environ. 36 (2002) 5543–5547.

[13] X. Tang, Y. Li, X. Huang, Y. Xu, H. Zhu, J. Wang, W. Shen, MnOx-CeO2 mixed oxide catalysts for complete oxidation of formaldehyde: effect of preparation method and calcination temperature, Appl. Catal. B: Environ. 62 (2006) 265–273.

[14] H. Chen, J. He, C. Zhang, H. He, Self-assembly of novel mesoporous manganese oxide nanostructures and their application in oxidative decomposition of formaldehyde, J. Phys. Chem. C 111 (2007) 18033–18038.

[15] Z. Wang, W. Wang, L. Zhang, D. Jiang, Surface oxygen vacancies on Co3O4 mediated catalytic formaldehyde oxidation at room temperature, Catal. Sci. Technol. 6 (2016) 3845–3853.

[16] Y. Huang, K. Ye, H. Li, W. Fan, F. Zhao, Y. Zhang, H. Ji, A highly durable catalyst based on CoxMn3-xO4 nanosheets for low-temperature formaldehyde oxidation,

[17] R. Fang, H. Huang, J. Jia, M. He, Q. Feng, Y. Zhan, D.Y.C. Leung, Efficient MnOx supported on coconut shell activated carbon for catalytic oxidation of indoor formaldehyde at room temperature, Chem. Eng. J. 334 (2018) 2050–2057.

[18] R.R. Hernandez, M.K. Hoffacker, C.B. Field, Efficient use of land to meet sustainable energy needs, Nat. Clim. Change 5 (2015) 353–358.

[19] X. Meng, Y. Li, J. Hou, M. Zeng, X. Zhao, Nanometals for solar-to-chemical energy conversion: From semiconductor-based photocatalysis to plasmon-mediated photocatalysis and photo-thermocatalysis, Adv. Mater. 28 (2016) 6781–6803.

[20] N. Zhou, V. Lopez-Puente, Q. Wang, L. Polavarapu, I. Pastoriza-Santos, Q. Xu, Plasmon-enhanced light harvesting: Applications in enhanced photocatalysis, photodynamic therapy and photovoltaics, RSC Adv. 5 (2015) 29076–29097.

[21] Z. Gan, X. Wu, M. Meng, X. Zhu, L. Yang, P.K. Chu, Photothermal contribution to enhanced photocatalytic performance of graphene-based nanocomposites, ACS Nano 8 (2014) 9304–9310.

[22] J. Zhang, Y. Li, L. Wang, C. Zhang, H. He, Catalytic oxidation of formaldehyde over manganese oxides with different crystal structures, Catal. Sci. Technol. 5 (2015) 2305–2313.

[23] J. Wang, P. Zhang, J. Li, C. Jiang, R. Yunus, J. Kim, Room-temperature oxidation of formaldehyde by layered manganese oxide: effect of water, Environ. Sci. Technol. 49 (2015) 12372–12379.

[24] J. Wang, J. Li, P. Zhang, G. Zhang, Understanding the "Seesaw Effect" of interlayered K^+ with different structure in manganese oxides for the enhanced formaldehyde oxidation, Appl. Catal., B: Environ. 224 (2018) 863–870.

[25] J. Wang, J. Li, C. Jiang, P. Zhou, P. Zhang, J. Yu, The effect of manganese vacancy in birnessite-type MnO2 on room-temperature oxidation of formaldehyde in air, Appl. Catal., B: Environ. 204 (2017) 147–155.

[26] J. Li, P. Zhang, J. Wang, M. Wang, Birnessite-type manganese oxide on granular activated carbon for formaldehyde removal at room temperature, J. Phys. Chem. C. 12 (2016) 24121–24129.

[27] S. Rong, P. Zhang, Y. Yang, L. Zhu, J. Wang, F. Liu, MnO2 framework for instantaneous mineralization of carcinogenic airborne formaldehyde at room temperature, ACS Catal. 7 (2017) 1057–1067.

[28] L. Brock, N. Duan, Z.R. Tian, O. Giraldo, H. Zhou, S.L. Suib, A review of porous manganese oxide materials, Chem. Mater. 10 (1998) 2619–2628.

[29] D.M. Robinson, Y.B. Go, M. Mui, G. Gardner, Z. Zhang, D. Mastrogiovanni, E. Garfunkel, J. Li, M. Greenblatt, D.C. Dismukes, Photochemical water oxidation by crystalline polymorphs of manganese oxides: structural requirements for catalysis, J. Am. Chem. Soc. 135 (2013) 3494–3501.

[30] F. Liu, M. Zeng, Y. Li, Y. Yang, M. Mao, X. Zhao, UV-Vis-Infrared light driven thermocatalytic activity of octahedral layered birnessite nanoflowers enhanced by a novel photoactivation, Adv. Funct. Mater. 26 (2016) 4518–4526.

[31] Y. Yang, Y. Li, M. Mao, M. Zeng, X. Zhao, UV-Visible-Infrared light driven thermocatalysis for environmental purification on aamsdellite MnO2 hollow spheres considerably promoted by a novel photoactivation, ACS Appl. Mater. Inter. 9 (2017) 2350–2357.

[32] Y. Zheng, W. Wang, D. Jiang, L. Zhang, X. Li, Z. Wang, Insights into the solar light driven thermocatalytic oxidation of VOCs over tunnel structured manganese oxides, Phys. Chem. Chem. Phys. 18 (2016) 18180–18186.

[33] H. Ren, M. Tang, B. Guan, K. Wang, J. Yang, F. Wang, M. Wang, J. Shan, Z. Chen, D. Wei, H. Peng, Z. Liu, Hierarchical graphene foam for efficient omnidirectional solar-thermal energy conversion, Adv. Mat. 29 (2017) 2590–2598.

[34] J.T. Robinson, S.M. Tabakman, Y. Liang, H. Wang, H.S. Casalongue, D. Vinh, H. Dai, Ultrasmall reduced gaphene oxide with high near-infrared absorbance for photothermal therapy, J. Am. Chem. Soc. 133 (2011) 6825–6831.

[35] X. Li, W. Xu, M. Tang, L. Zhou, B. Zhu, S. Zhu, J. Zhu, Graphene oxide-based efficient and scalable solar desalination under one sun with a confined 2D water path, Proc. Natl. Acad. Sci. U. S. A. 113 (2016) 13953–13958.

[36] G. Yu, L. Hu, M. Vosgueritchian, H. Wang, X. Xie, J.R. McDonough, X. Cui, Y. Cui, Z. Bao, Solution-processed Graphene/MnO2 nanostructured textiles for high-performance electrochemical capacitors, Nano Lett. 11 (2011) 2905–2911.

[37] Z. Wu, W. Ren, D. Wang, F. Li, B. Liu, H. Cheng, High-energy MnO2 nanowire/graphene and graphene asymmetric electrochemical capacitors, ACS Nano 4 (2010) 5835–5842.

[38] S. Yang, X. Song, P. Zhang, L. Gao, Facile synthesis of nitrogen-doped graphene-ultrathin MnO2 sheet composites and their electrochemical performances, ACS Appl. Mater. Interfaces 5 (2013) 3317–3322.

[39] S. Chen, J. Zhu, X. Wu, Q. Han, X. Wang, Graphene oxide-MnO2 nanocomposites for supercapacitors, ACS Nano 4 (2010) 2822–2830.

[40] S. Winnerl, M. Orlita, P. Plochocka, P. Kossacki, M. Potemski, T. Winzer, E. Malic, A. Knorr, M. Sprinkle, C. Berger, W.A. Heer, F. Schneider, M. Helm, Carrier relaxation in epitaxial graphene photoexcited near the Dirac point, Phys. Rev. Lett. 107 (2011) 237401.

[41] Y. Tian, H. Tian, Y. Wu, L. Zhu, L. Tao, W. Zhang, Y. Shu, D. Xie, Y. Yang, Z. Wei, X. Lu, T. Ren, C. Shih, Z. Zhao, Coherent generation of photo-thermo-acoustic wave from graphene sheets, Sci. Rep. 5 (2015) 10582.

[42] L.Y. Gan, Q. Zhang, C.S. Guo, U. Schwingenschlogl, Y. Zhao, Two-dimensional MnO2/Graphene interface: half-metallicity and quantum anomalous hall state, J Phys. Chem. C 120 (2016) 2119–2125.

[43] L. Peng, X. Peng, B. Liu, C. Wu, Y. Xie, G. Yu, Ultrathin two-dimensional MnO2/Graphene hybrid nanostructures for high-performance, flexible planar supercapacitors, Nano Lett. 13 (2013) 2151–2157.

[44] K. Li, J. Chen, Y. Peng, W. Li, T. Yan, J. Li, The relationship between surface open cells of α-MnO2 and CO oxidation ability from a surface point of view, J. Mater. Chem. A Mater. Energy Sustain. 5 (2017) 20911–20921.

[45] L. Lu, H. Tian, J.He Q. Yang, Graphene-MnO2 hybrid nanostructure as a new

catalyst for formaldehyde oxidation, J. Phys. Chem. C 120 (2016) 23660–23668.

[46] I.Y. Jeon, H.J. Choi, S.M. Jung, J.M. Seo, M.L. Kim, L. Dai, J.B. Baek, Large-Scale production of edge-selectively functionalized graphene nanoplatelets via ball milling and their use as metal-free electrocatalysts for oxygen reduction reaction, J. Am. Chem. Soc. 135 (2013) 1386–1393.

[47] I.Y. Jeon, H.J. Choi, M. Choi, J.M. Seo, S.M. Jung, M.J. Kim, S. Zhang, L. Zhang, Z. Xia, L. Dai, N. Park, J.B. Baek, Facile, scalable synthesis of edge-halogenated graphene nanoplatelets as efficient metal-free eletrocatalysts for oxygen reduction reaction, Sci. Report 3 (2013) 1810.

[48] C. Julien, M. Massot, R. Baddour-Hadjean, S. Franger, S. Bach, J.P. Pereira-Ramos, Raman spectra of birnessite manganese dioxides, Solid State Ion. 159 (2003) 345–356.

[49] T. Szabo, O. berkesi, I. Dekany, DRIFT study of deuterium-exchanged graphite oxide, Carbon 43 (2005) 3186–3189.

[50] P. Lian, X. Zhu, S. liang, Z. Li, W. Yang, H. Wang, Large reversible capacity of high quality graphene sheets as an anode material for lithium-ion batteries, Electrochim. Acta 55 (2010) 3909–3914.

[51] G.M. Neelgund, A.R. Oki, Influence of carbon nanotubes and graphene nanosheets on photothermal effect of hydroxyapatite, J. Colloid Interf. Sci. 484 (2016) 135–145.

[52] Y. Chen, Y. Su, S. Hu, S. Chen, Functionalized graphene nanocomposites for enhancing photothermal therapy in tumor treatment, Adv. Drug Deliver. Rev. 105 (2016) 190–204.

[53] G.I. Panov, A.K. Uriarte, M.A. Rodkin, V.I. Sobolev, Generation of active oxygen species on solid surfaces. Opportunity for novel oxidation technologies over zeolites, Catal. Today 41 (1998) 365–385.

[54] Y. Chen, Z. Huang, M. Zhou, Z. Ma, J. Chen, X. Tang, Single silver adatoms on nanostructured manganese Oxide surfaces: boosting oxygen activation for benzene abatement, Environ. Sci. Technol. 51 (2017) 2304–2311.

[55] J. Zhao, J. Nan, Z. Zhao, N. Li, J. Liu, F. Cui, Energy-efficient fabrication of a novel multivalence Mn_3O_4-MnO_2 heterojunction for dye degradation under visible light irradiation, Appl. Catal., B: Environ. 202 (2017) 509–517.

[56] W. Yang, Y. Zhu, F. You, L. Yan, Y. Ma, C. Lu, P. Gao, Q. Hao, W. Li, Insights into the surface-defect dependence of molecular oxygen activation over birnessite-type MnO_2, Appl. Catal., B: Environ. 233 (2018) 184–193.

[57] A. Tilocca, A. Selloni, O2 and vacancy diffusion on rutile (110): pathways and electronic properties, ChemPhysChem 6 (2005) 1911–1916.